Control of an Atomic Quadrupole Transition in a Phase-Stable Standing Wave

Alfredo Ricci Vasquez,[1,*] Carmelo Mordini,[1] Chloé Vernière,[1] Martin Stadler,[1] Maciej Malinowski,[1] Chi Zhang,[1] Daniel Kienzler,[1] Karan K. Mehta,[1,†] and Jonathan P. Home[1,2,‡]
[1]*Institute for Quantum Electronics, ETH Zürich, 8093 Zürich, Switzerland*
[2]*Quantum Center, ETH Zürich, 8093 Zürich, Switzerland*

(Received 10 October 2022; revised 19 December 2022; accepted 31 January 2023; published 27 March 2023)

Using a single calcium ion confined in a surface-electrode trap, we study the interaction of electric quadrupole transitions with a passively phase-stable optical standing wave field sourced by photonics integrated within the trap. We characterize the optical fields through spatial mapping of the Rabi frequencies of both carrier and motional sideband transitions as well as ac Stark shifts. Our measurements demonstrate the ability to engineer favorable combinations of sideband and carrier Rabi frequency as well as ac Stark shifts for specific tasks in quantum state control and metrology.

DOI: 10.1103/PhysRevLett.130.133201

Light-matter interaction is a topic of fundamental interest, which lies at the heart of our technological capability to control quantum matter. The strongest interactions are due to coupling of the field to the electric dipole moment, which exhibit coupling rates dependent on the electric field strength and polarization. These have diverse applications, including laser cooling and optical trapping [1–3]. When dipole coupling is forbidden by symmetry, electric quadrupole terms can become dominant. Because of their narrow linewidths, such transitions have found an important role in quantum simulation of interacting systems [4], metrology [5–7], precision measurement [8], and quantum computing [9,10] with both neutral atoms and atomic ions. Quadrupole transitions are driven by electric field gradients, which means that the matrix elements have a deeper tensorial structure than for dipole transitions, as illustrated in various studies, including those of the interaction of single ions with structured light fields [11–13].

Spatial structuring of light fields, achieved through phase-stable interference, is widely used in atomic physics experiments with neutral atoms [14,15]. Standing waves may also carry advantages for quantum information processing with trapped ions, where spatial structure can be exploited to control the coupling of an atom by tuning its position inside the field. Driving transitions in a region of zero electric field suppress any Stark shifts due to nonresonant dipole couplings. These features can be relevant in the context of achieving faster entangling gates [16,17], for applying spin-dependent forces [18], and for metrology [19]. However, these applications require a phase-stable standing wave, which must be positioned precisely relative to the position of the ion. Such control has been achieved with free space laser beams using active feedback stabilization [20], using reflections from the trap surface [21], or using a standing wave produced by a high-finesse optical cavity [11]. However, all of these approaches pose significant challenges for scaling systems up to many laser beams, such as will be required for high-performance quantum computation, compact atomic clocks, or sensing.

In this Letter, we demonstrate control of a $^{40}Ca^{+}$ ion quadrupole transition in a phase-stable standing wave [22–25] generated through the use of integrated optics: An on-chip waveguide splitter feeds two grating output couplers which emit into free space. The resulting optical field is a standing wave in the direction parallel to the chip plane and a traveling wave in the direction perpendicular to the chip, which causes a spatial variation in the relative strength of the allowed transitions dependent on the ion position inside the electric field pattern. We characterize the matrix elements of the allowed transitions of the trapped ion as a function of its position. We separate for each of them the strength of the resonant coupling measured by the Rabi frequency Ω from the ac Stark shift induced by nonresonant excitations. We explore the relation between carrier transitions and the corresponding sidebands along the axial motional mode aligned with the direction of the standing wave and find positions with favorable properties, e.g., offering sideband transitions with no accompanying carrier excitation nor ac Stark shift. This provides the basis for exploiting such a light field for quantum computation, choosing the suitable ion position to suppress unwanted off-resonant effects in gates performed on the optical qubit of the ion.

Figure 1 shows the geometry of the trap and the transitions relevant for our experiment. Two grating outcouplers aligned along the trap axis x each emit a Gaussian-like laser beam at 729 nm propagating at an angle $\alpha = 37°$ from the normal to the trap plane z. The beams intersect at a height of 50 μm above the chip where an ion is trapped, creating the standing wave interference pattern. Both laser beams are linearly polarized along the y

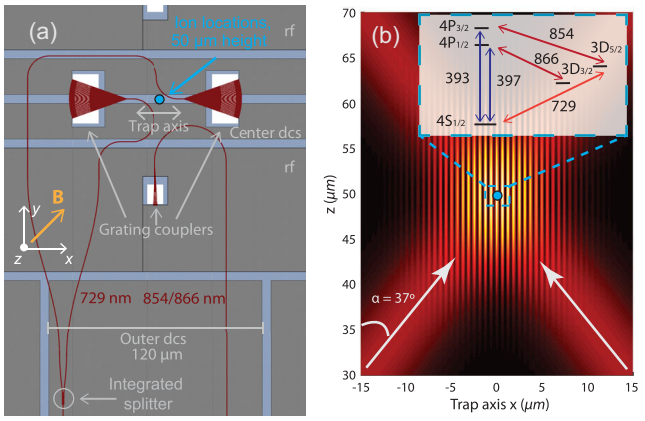

FIG. 1. (a) Trap layout schematic. Two grating couplers emit two 729-nm beams generated using an integrated waveguide splitter. The off-axis coupler is used for 854- and 866-nm repump light. Near-UV light is sent through free space. The ion is trapped 50 μm above the position of the blue dot. A set of dc electrodes is used to position the ion along the trap axis (x) with a resolution on the order of ~10 nm. (b) Schematic of the intensity profile of the light field along the xz plane near the position of the ion. The inset shows the electronic structure of the $^{40}Ca^{+}$ ion, where the numbers are the wavelengths of the transitions in nanometers. Zeeman sublevels are not shown.

direction, and the resulting field can be described in the vicinity of the ion as a combination of two plane waves:

$$\mathbf{E}(\mathbf{r}) = E_0 e^{ik_z z}\cos(k_x \Delta x)\mathbf{e}_y, \tag{1}$$

where $k_x = k\sin(\alpha)$ and $k_z = k\cos(\alpha)$ are the components of the beam wave vector, x is the ion position, $k = 2\pi/\lambda$, $\mathbf{e}_y$ is the unit vector along y, and $\Delta x = (x - x_0)$, where x_0 accounts for the shift in the standing wave phase relative to the coordinate system.

This field is used to drive quadrupole transitions between our chosen ground state $|4S_{1/2}, m_j = -1/2\rangle = |g\rangle$ and the $3D_{5/2}$ level. Multiple transitions exist from $|g\rangle$ to states in the $3D_{5/2}$ manifold differing in their magnetic quantum number by Δm_j, each of which are spectrally resolved. For a given component with resonant frequency ω_o, the strongest resonant excitations (carrier transitions) occur when the laser frequency $\omega_l = \omega_o$, resulting in the Hamiltonian $\hat{H}_c = (\hbar/2)(\Omega_c\hat{\sigma}_+ + \text{H.c.})$, where $\hat{\sigma}_+ = |e\rangle\langle g|$ and $\hat{\sigma}_- = |g\rangle\langle e|$ are the atomic raising and lowering operators, respectively, and Ω_c is the carrier Rabi frequency, given by

$$\Omega_c = \frac{eE_0}{\hbar}\mathbf{F}(\Delta m_j, \mathbf{B})\cdot\boldsymbol{\kappa}_c(x), \tag{2}$$

where $\boldsymbol{\kappa}_c = \{-\sin(\alpha)\sin(k_x\Delta x), 0, i\cos(\alpha)\cos(k_x\Delta x)\}$ encodes the gradient of the electric field as a function of the ion position and the matrix elements $F_a(\Delta m_j, \mathbf{B}) = (k/2)\langle e|\hat{r}_a\hat{r}_y|g\rangle$ depend on the change in the magnetic quantum number in the selected transition Δm_j, as well as the direction of the external magnetic field $\mathbf{B} = (\mathbf{e}_x + \mathbf{e}_y)/\sqrt{2}$ defining the quantization axis. In this configuration, at the antinodes of the standing wave (i.e., $k_x\Delta x = p\pi$, $p \in \mathbb{Z}$) there are only gradients of the fields in the out-of-plane z direction which are maximized at this position. At the nodes ($k_x\Delta x = \pm[p + 1/2]\pi$), there are only gradients of the fields along the trap axis x direction, which are maximized at this position. Explicit calculation of the matrix elements gives $F_z(\Delta m_j = 0) = F_x(\Delta m_j = \pm 1) = 0$ such that at the antinodes the carrier transition with $\Delta m_j = 0$ is suppressed while the $\Delta m_j = \pm 1$ transitions are maximized. The opposite happens at the nodal positions. Furthermore, the relative phase of 90° between $F_z(\Delta m_j = \pm 2)$ and $F_x(\Delta m_j = \pm 2)$ allows one to tune the coupling strength of these transitions, maximizing (and minimizing) them in between the nodes and antinodes of the standing wave. Detailed calculations of the matrix elements F_a are provided in Supplemental Material [26].

Since the center of mass of the ion oscillates in its confining potential, the laser light is phase modulated in the rest frame of the atom, and the spectrum of the light-matter interaction exhibits motional sidebands. Tuning the laser frequency to the blue sideband of a given transition $\omega_l = \omega_o + \omega_x$, where ω_x denotes the axial trapping frequency, produces the Hamiltonian $\hat{H}_{\text{bsb}} = (\hbar/2)(\Omega_s\hat{a}^\dagger\hat{\sigma}_+ + \text{H.c.})$. Here, $\Omega_s = a_x\partial_x\Omega_c$ is the sideband Rabi frequency, which is defined by the spatial gradient of the carrier coupling along the respective oscillation direction, $a_x = \sqrt{\hbar/2m\omega_x}$ is the zero point motion root-mean-square amplitude, and $\hat{a}^\dagger$ and $\hat{a}$ are the creation and annihilation operators, respectively, of the oscillator. In the standing wave, the electric field gradient and its derivative along the trap axis are out of phase; therefore, for any given transition, $|\Omega_s|$ is maximized when $|\Omega_c|$ is at a minimum and vice versa. This means that the logic regarding the transition Rabi frequency at nodes and antinodes given above for the carrier transitions is reversed for the sidebands. Careful choice of the transition allows suppression of unwanted couplings while implementing a desired Hamiltonian.

We probe the generated light field by placing the ion at different positions along the trap axis and measuring the respective Rabi frequencies. Each repetition of the experiment, we cool the axial motional mode of the ion near the ground state ($\bar{n}_x \sim 1$ quanta) and prepare the electronic state in $|g\rangle$ via optical pumping. We then excite the transition of interest using a fixed duration pulse of the standing wave and subsequently measure the ion electronic state using state-dependent fluorescence. This sequence is repeated multiple times for each experimental setting to gain statistics. Rabi frequencies for carrier transitions are

extracted from the time of minimum occupation of $|g\rangle$, with a precalibrated correction for finite switching times of the pulse (see Supplemental Material [26]). For sideband transitions, we extract the Rabi frequency from multiple Rabi oscillations assuming a thermal distribution of the excited motional mode (see Supplemental Material [26]). We perform experiments at positions separated by 15.7 nm over a full period of the standing wave. For each position, we probe three of the allowed transitions $|g\rangle \leftrightarrow |3D_{5/2}, m_j = -5/2, -3/2, -1/2\rangle$ that have $\Delta m_j = -2, -1, 0$, respectively. In our magnetic field of 5.8 G, the carrier transitions are separated by ~9.7 MHz, and the trap frequency is $\omega_x = (2\pi) \times 1.64$ MHz.

Figure 2 shows the measured Rabi frequencies for carriers and sidebands, compared with theoretical predictions. We see broad agreement between experiment and theory for both datasets. We fit Eq. (2) to the data for $\Delta m_j = 0$ with E_0 and x_0 floated and the orientation of the magnetic field fixed to $\mathbf{B}$. The fit is plotted as well as the resulting predictions for the other transitions (solid curves). There are observable discrepancies between these predictions and the data. We found that these can be reduced by adjusting the direction of the magnetic field in the model by 2°–3° in both the x-y and the x-z planes (dashed lines). This adjustment is consistent with uncertainties in the magnetic field direction estimated previously in this setup [37]. As expected, the minimum values for the excitation of carrier happen when the sideband excitation is maximized. At these positions, the carrier Rabi frequencies are suppressed relative to their maximal values by 14.07(6)×, 16.9(1)×, and 35.9(4)× for $\Delta m_j = 0, -1, -2$, respectively. We have observed suppression factors up to 300× but do not find that this is repeatable. This is likely due to slight changes in the exact orientation of the magnetic field, for which the transition with $\Delta m_j = 0$ has the highest sensitivity and the transition with $\Delta m_j = -2$ has the lowest, in agreement with our observations. The measurements of the sideband Rabi frequencies exhibit higher uncertainties than the carrier counterparts given their dependence on the phonon occupation which follows a shot-to-shot thermal distribution. Also, since $|\Omega_s|$ is $\eta = k_x a_x \sim 0.05$ times lower than $|\Omega_c|$, $|\Omega_s|$ is more sensitive to detunings arising from miscalibration in the carrier transition frequency, ac Stark shift, and trap frequency.

When resonantly exciting one of the transitions between the $4S_{1/2}$ and $3D_{5/2}$ manifolds, all the other transitions in the ion are driven off-resonantly. This results in a net ac Stark shift of the desired transition [38]. The main contribution to the ac Stark shift comes from off-resonantly driving $3D_{5/2} \leftrightarrow 4P_{3/2}$, $4S_{1/2} \leftrightarrow 4P_{1/2}$, and $4S_{1/2} \leftrightarrow 4P_{3/2}$ transitions, which are all dipole allowed and, therefore, proportional to the intensity of the field, while a second contribution applies from off-resonantly exciting other quadrupole transitions in the $4S_{1/2} \leftrightarrow 3D_{5/2}$ manifold [see Fig. 1(b)]. At the node of the standing wave, we can maximally drive the carrier transition with $\Delta m_j = 0$ or for the sideband transition with $\Delta m_j = -1$, allowing us to suppress the dipole contribution of the ac Stark shifts. When maximally driving any sideband, the dominant ac Stark shift contribution from off-resonantly driving the carrier is suppressed. Figure 3 shows the measured ac Stark shifts for the carrier and the sidebands. Around the nodal position where the $\Delta m_j = 0$ carrier and the $\Delta m_j = -1$ sideband are strongly driven, we observe a high suppression of the ac Stark shift for both transitions. The observed residual shift is due to off-resonant couplings to neighboring quadrupole transitions. In practice, this residual quadrupole ac Stark shift could be minimized by increasing the Zeeman splitting with higher magnetic fields. Detailed calculations on the separate contributions of the dipole and

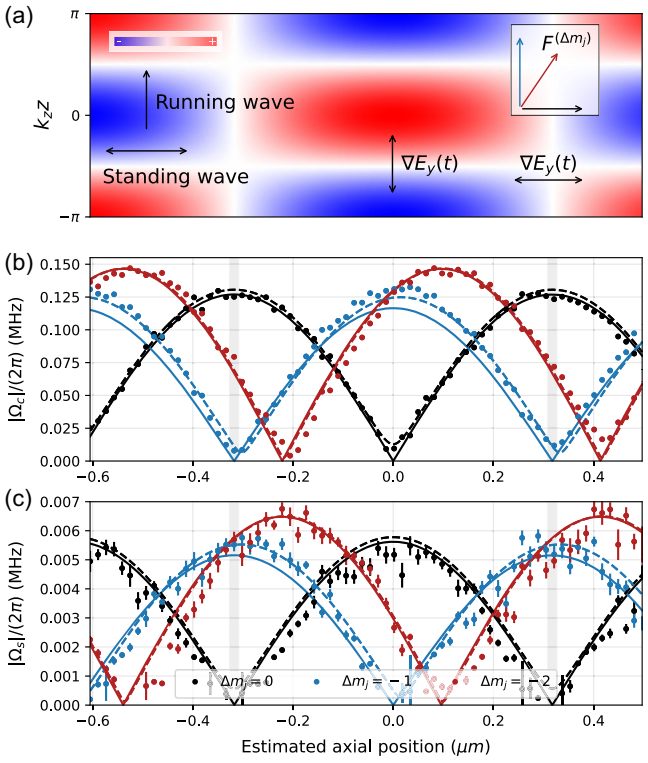

FIG. 2. (a) Sketch of the spatial dependence of the y-polarized electric field [Eq. (1)] as a function of z and x at a fixed instant in time. The arrows indicate the direction of the electric field gradient. The box in the top right corner indicates the directions of the magnitude of the components of $\mathbf{F}(\Delta m_j)$ in the xz plane, with colors chosen to match the respective datasets in (b) and (c). (b),(c) Measurements of absolute value of the carrier (b) and blue sideband (c) Rabi frequencies as a function of the ion position. Solid lines plot predictions from the theoretical model in Eq. (2) with the nominal orientation of the magnetic field, while dashed lines include a correction for the magnetic field orientation of 2.7° and 3.1° for the out-of- and in-plane directions, respectively. Two shaded lines are used to denote the positions of the nodes of the standing wave.

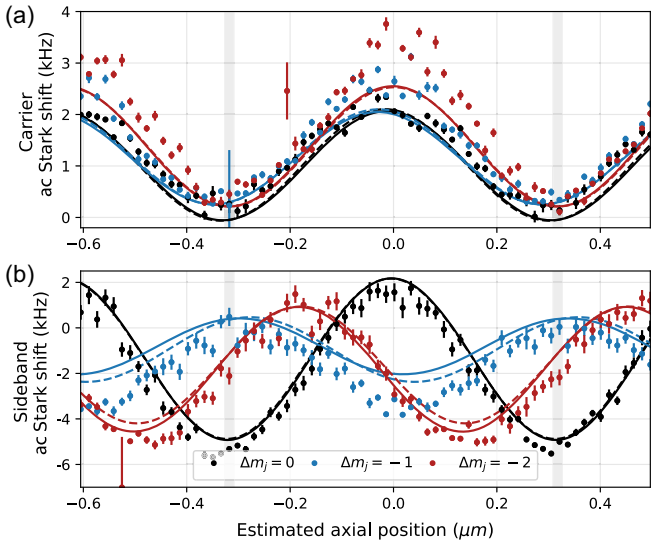

FIG. 3. Measurements of the ac Stark shifts on the carrier (a) and on the sideband transitions (b) as a function of the ion position in a period of the standing wave. Solid lines are computed using the nominal magnetic field orientation and the amplitude of the light field obtained from the Rabi frequency pattern of the transition with $\Delta m_j = 0$. Dashed lines include a correction for the magnetic field orientation.

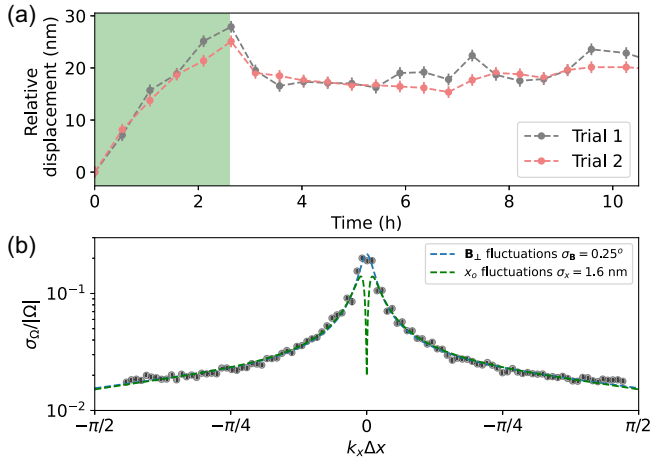

FIG. 4. (a) shows the relative displacement of the ion position with respect to the standing wave pattern over time (x_0). Two repetitions of the same experiment performed in different days are shown. The green region shows the time span where 5 min of exposure to PI light was interleaved between measurements. (b) shows the relative standard deviation of the $\Delta m_j = 0$ Rabi frequency as a function of the position of the ion in the standing wave. Lines show two different fits, corresponding to Rabi frequency fluctuation coming from position or magnetic field orientation fluctuations.

quadrupole ac Stark shifts can be found in Supplemental Material [26].

The use of integrated photonics provides a reliable way of passively controlling the relative phase of the beams generating the standing wave. The degree with which the ion can be placed with respect to the standing wave is limited by stray electric fields. We studied the stability of this positioning by repeatedly recording the carrier Rabi frequency pattern and measuring the displacement of the ion with respect to the standing wave pattern during 10 h. The primary cause of shifts is due to ultraviolet light at 389 and 423 nm used for loading ions by photoionization. This is illustrated in Fig. 4(a), which shows the fitted value of x_0. Between each of the first five measurements, we turn on the photoionization (PI) beams for a 5-min duration. On both trials, we see a similar drift while the PI light is on and residual drift at the level of ~10nm when it is off. The position displacement tends to saturate after a few cycles of exposure to PI light and is then followed by a discharge process that occurs within the first hours but leaves a permanent displacement over longer timescales. This behavior was repeatable over several trials. The dependence of the fitted x_0 on the presence of PI light suggests that the origin of the displacement is dominated by drifts in the ion position rather than shifts in the relative phase between the beams forming the standing wave [39].

At timescales faster than those required to obtain a single Rabi frequency, changes in the ion position would produce decay in the observed Rabi oscillations. We measured the decay of the Rabi oscillations as a function of the position of the ion in the standing wave for the carrier transition with $\Delta m_j = 0$. Assuming shot-to-shot fluctuations of the Rabi frequency sampled from a Gaussian distribution with width σ_Ω, the population of the $|S_{1/2}\rangle$ state as a function of time is found to be $P(|S_{1/2}\rangle) = 0.5 + 0.5\exp(-\sigma_\Omega^2 t^2/2)\cos(|\Omega|t)$. Extracted values of the fractional Rabi frequency fluctuations $\sigma_\Omega/|\Omega|$ as a function of the position of the ion are shown in Fig. 4(b), exhibiting increased Rabi frequency fluctuations around $k_x \Delta x = 0$. We fit these results with two different models, where fluctuations of the Rabi frequency are produced by fluctuations of (i) the out-of-plane direction of the magnetic field or (ii) small displacements between the ion and the light field. Both models produce satisfactory fits, allowing us to bound the shot-to-shot magnetic field fluctuations to $\sigma_\mathbf{B} = 0.25°$ or, alternatively, the position fluctuations to $\sigma_x = 1.6$ nm, the latter representing a fluctuation of ~0.13% of the period of the standing wave, arising from either changes of the relative phase between the two beams or drifts in the ion position. The offset to the curve due to Rabi frequency fluctuations on the order of $\sigma_\Omega/|\Omega| \sim 1.5\%$ is consistent with the expected thermal occupation of the atomic center of mass motion [40]. Thermal effects in the carrier Rabi frequency can be accounted by considering higher-order terms in the Lamb-Dicke expansion, which modify the carrier Rabi frequency to $\Omega_c(n) \approx \Omega_c[1 - \eta^2(2n+1)/2]$ for a given Fock state n. Since the fluctuations are proportional to the

Rabi frequency, the fractional fluctuations are independent of position.

Our Letter offers insight in the physics of atom-light interaction at a fundamental level and demonstrates the use of integrated photonics to create structured light fields with chosen properties that can be exploited advantageously for quantum computing and metrology. Specifically, the possibility of precisely locating an ion in the standing wave without constant recalibration or active feedback allows us to envision the use of such a device in large-scale quantum information processors. In the specific field configuration employed here, the choice of the $\Delta m_j = -1$ transitions maximizes sideband Rabi frequency at intensity nulls, where ac Stark shifts are minimal and the carrier transition is suppressed. For quantum gates driven by motional sidebands, this offers a route to reduced off-resonant contributions to gate errors. The carrier transition with lowest magnetic field sensitivity ($\Delta m_j = 0$) is driven with maximal strength at the nodes of the standing wave, facilitating use for optical clocks with reduced sensitivity to ac Stark shifts. All of these features are available in an integrated form, which greatly facilitates scaling and portability.

We acknowledge funding from the Swiss National Science Foundation (Grant No. 200020_207334), the EU H2020 FET Open project PIEDMONS (Grant No. 801285), the National Centre of Competence in Research for Quantum Science and Technology (QSIT) (Grant No. 51NF40-185902), and the EU Quantum Flagship H2020-FETFLAG-2018-03 (Grant Agreement No. 820495 AQTION). D. K. acknowledges support from the Swiss National Science Foundation (Ambizione Grant No. PZ00P2_179909). K. K. M. acknowledges support from an ETH Postdoctoral fellowship. We acknowledge LioniX International for fabrication of the trap devices.

K. K. M. conceived the experiment and designed the device. Experimental data were taken by A. R. V. and C. M., using an apparatus with significant contributions from M. M., C. Z., M. S., and K. K. M. Data analysis and modeling were performed by A. R. V., C. V., and C. M. The paper was written by A. R. V. and C. M. with input from all authors. The work was supervised by D. K. and J. P. H.

*aricci@ethz.ch
†Present address: School of Electrical and Computer Engineering, Cornell University, Ithaca, New York 14853, USA.
‡jhome@ethz.ch

[1] W. D. Phillips, J. V. Prodan, and H. J. Metcalf, Laser cooling and electromagnetic trapping of neutral atoms, J. Opt. Soc. Am. B **2**, 1751 (1985).
[2] R. Grimm, M. Weidemüller, and Y. B. Ovchinnikov, Optical Dipole Traps for Neutral Atoms (Academic Press, New York, 2000), pp. 95–170, 10.1016/S1049-250X(08)60186-X.
[3] J. Eschner, G. Morigi, F. Schmidt-Kaler, and R. Blatt, Laser cooling of trapped ions, J. Opt. Soc. Am. B **20**, 1003 (2003).
[4] R. Blatt and C. F. Roos, Quantum simulations with trapped ions, Nat. Phys. **8**, 277 (2012).
[5] A. D. Ludlow, M. M. Boyd, J. Ye, E. Peik, and P. O. Schmidt, Optical atomic clocks, Rev. Mod. Phys. **87**, 637 (2015).
[6] T. Ray, R. K. Gupta, V. Gokhroo, J. L. Everett, T. Nieddu, K. S. Rajasree, S. N. Chormaic, and S. N. Chormaic, Observation of the ^{87}Rb $5S_{1/2}$ to $4D_{3/2}$ electric quadrupole transition at 516.6 nm mediated via an optical nanofibre, New J. Phys. **22**, 062001 (2020).
[7] S. Tojo, M. Hasuo, and T. Fujimoto, Absorption Enhancement of an Electric Quadrupole Transition of Cesium Atoms in an Evanescent Field, Phys. Rev. Lett. **92**, 053001 (2004).
[8] Q. Zhang, Y. Wang, C. Zhu, Y. Wang, X. Zhang, K. Gao, and W. Zhang, Precision measurements with cold atoms and trapped ions, Chin. Phys. B **29**, 093203 (2020).
[9] D. Leibfried, R. Blatt, C. Monroe, and D. Wineland, Quantum dynamics of single trapped ions, Rev. Mod. Phys. **75**, 281 (2003).
[10] C. D. Bruzewicz, J. Chiaverini, R. McConnell, and J. M. Sage, Trapped-ion quantum computing: Progress and challenges, Appl. Phys. Rev. **6**, 021314 (2019).
[11] A. B. Mundt, A. Kreuter, C. Becher, D. Leibfried, J. Eschner, F. Schmidt-Kaler, and R. Blatt, Coupling a Single Atomic Quantum Bit to a High Finesse Optical Cavity, Phys. Rev. Lett. **89**, 103001 (2002).
[12] C. T. Schmiegelow, J. Schulz, H. Kaufmann, T. Ruster, U. G. Poschinger, and F. Schmidt-Kaler, Transfer of optical orbital angular momentum to a bound electron, Nat. Commun. **7**, 1 (2016).
[13] M. Drechsler, S. Wolf, C. T. Schmiegelow, and F. Schmidt-Kaler, Optical Superresolution Sensing of a Trapped Ion's Wave Packet Size, Phys. Rev. Lett. **127**, 143602 (2021).
[14] C. Gross and I. Bloch, Quantum simulations with ultracold atoms in optical lattices, Science **357**, 995 (2017).
[15] S. Subhankar, Y. Wang, T.-C. Tsui, S. L. Rolston, and J. V. Porto, Nanoscale Atomic Density Microscopy, Phys. Rev. X **9**, 021002 (2019).
[16] K. K. Mehta, C. Zhang, S. Miller, and J. P. Home, Towards fast and scalable trapped-ion quantum logic with integrated photonics, in *Advances in Photonics of Quantum Computing, Memory, and Communication XII*, edited by P. R. Hemmer, A. L. Migdall, and Z. U. Hasan, International Society for Optics and Photonics Vol. 10933 (SPIE, Bellingham, WA, 2019), pp. 24–34, 10.1117/12.2507647.
[17] A. Sørensen and K. Mølmer, Entanglement and quantum computation with ions in thermal motion, Phys. Rev. A **62**, 022311 (2000).
[18] B. de Neeve, T. L. Nguyen, T. Behrle, and J. P. Home, Error correction of a logical grid state qubit by dissipative pumping, Nat. Phys. **18**, 296 (2022).
[19] N. Huntemann, M. Okhapkin, B. Lipphardt, S. Weyers, C. Tamm, and E. Peik, High-Accuracy Optical Clock Based on the Octupole Transition in Yb + 171, Phys. Rev. Lett. **108**, 090801 (2012).

[20] C. T. Schmiegelow, H. Kaufmann, T. Ruster, J. Schulz, V. Kaushal, M. Hettrich, F. Schmidt-Kaler, and U. G. Poschinger, Phase-Stable Free-Space Optical Lattices for Trapped Ions, Phys. Rev. Lett. **116**, 033002 (2016).

[21] T. E. Delaubenfels, K. A. Burkhardt, G. Vittorini, J. T. Merrill, K. R. Brown, and J. M. Amini, Modulating carrier and sideband coupling strengths in a standing-wave gate beam, Phys. Rev. A **92**, 061402(R) (2015).

[22] K. K. Mehta, C. D. Bruzewicz, R. McConnell, R. J. Ram, J. M. Sage, and J. Chiaverini, Integrated optical addressing of an ion qubit, Nat. Nanotechnol. **11**, 1066 (2016).

[23] R. J. Niffenegger, J. Stuart, C. Sorace-Agaskar, D. Kharas, S. Bramhavar, C. D. Bruzewicz, W. Loh, R. T. Maxson, R. McConnell, D. Reens, G. N. West, J. M. Sage, and J. Chiaverini, Integrated multi-wavelength control of an ion qubit, Nature (London) **586**, 538 (2020).

[24] K. K. Mehta, C. Zhang, M. Malinowski, T.-L. Nguyen, M. Stadler, and J. P. Home, Integrated optical multi-ion quantum logic, Nature (London) **586**, 533 (2020).

[25] M. Ivory, W. J. Setzer, N. Karl, H. McGuinness, C. DeRose, M. Blain, D. Stick, M. Gehl, and L. P. Parazzoli, Integrated Optical Addressing of a Trapped Ytterbium Ion, Phys. Rev. X **11**, 041033 (2021).

[26] See Supplemental Materials at http://link.aps.org/supplemental/10.1103/PhysRevLett.130.133201, which contains Refs. [27–36] for further details regarding the calculations of the Rabi frequencies and ac Stark shifts, the experimental apparatus and the experimental sequence.

[27] Y. Zhang, S. Yang, A. E.-J. Lim, G.-Q. Lo, C. Galland, T. Baehr-Jones, and M. Hochberg, A compact and low loss y-junction for submicron silicon waveguide, Opt. Express **21**, 1310 (2013).

[28] J. D. Jackson, *Classical Electrodynamics* (John Wiley & Sons, Inc., New York, 1962).

[29] D. F. James, Quantum dynamics of cold trapped ions with application to quantum computation, Appl. Phys. B **66**, 181 (1998).

[30] P. A. Barton, C. J. Donald, D. M. Lucas, D. A. Stevens, A. M. Steane, and D. N. Stacey, Measurement of the lifetime of the $3d^2D_{5/2}$ state in $^{40}Ca^+$, Phys. Rev. A **62**, 032503 (2000).

[31] N. B. Delone and V. P. Krainov, AC stark shift of atomic energy levels, Phys. Usp. **42**, 669 (1999).

[32] M. Grau, https://atomphys.org.

[33] R. Lechner, C. Maier, C. Hempel, P. Jurcevic, B. P. Lanyon, T. Monz, M. Brownnutt, R. Blatt, and C. F. Roos, Electromagnetically-induced-transparency ground-state cooling of long ion strings, Phys. Rev. A **93**, 053401 (2016).

[34] H. Häffner, C. F. Roos, and R. Blatt, Quantum computing with trapped ions, Phys. Rep. **469**, 155 (2008).

[35] D. M. Meekhof, C. Monroe, B. E. King, W. M. Itano, and D. J. Wineland, Generation of Nonclassical Motional States of a Trapped Atom, Phys. Rev. Lett. **76**, 1796 (1996).

[36] L. B. Soldano and E. C. Pennings, Optical multi-mode interference devices based on self-imaging: Principles and applications, J. Lightwave Technol. **13**, 615 (1995).

[37] C. Zhang, Scalable technologies for surface-electrode ion traps, Ph.D. thesis, ETH Zurich, 2022, 10.3929/ethz-b-000536415.

[38] H. Häffner, S. Gulde, M. Riebe, G. Lancaster, C. Becher, J. Eschner, F. Schmidt-Kaler, and R. Blatt, Precision Measurement and Compensation of Optical Stark Shifts for an Ion-Trap Quantum Processor, Phys. Rev. Lett. **90**, 143602 (2003).

[39] M. Harlander, M. Brownnutt, W. Hänsel, and R. Blatt, Trapped-ion probing of light-induced charging effects on dielectrics, New J. Phys. **12**, 093035 (2010).

[40] M. Malinowski, Unitary and dissipative trapped-ion entanglement using integrated optics, Ph.D. thesis, ETH Zurich, 2021, 10.3929/ethz-b-000516613.